

Bandgap tuning of multiferroic oxide solar cells

R. Nechache^{1,2*}, C. Harnagea², S. Li², L. Cardenas², W. Huang², J. Chakrabartty² and F. Rosei^{2,3*}

Multiferroic films are increasingly being studied for applications in solar energy conversion because of their efficient ferroelectric polarization-driven carrier separation and above-bandgap generated photovoltages, which in principle can lead to energy conversion efficiencies beyond the maximum value (~34%) reported in traditional silicon-based bipolar heterojunction solar cells. However, the efficiency reported so far is still too low (<2%) to be considered for commercialization. Here, we demonstrate a new approach to effectively tune the bandgap of double perovskite multiferroic oxides by engineering the cationic ordering for the case of $\text{Bi}_2\text{FeCrO}_6$. Using this approach, we report a power conversion efficiency of 8.1% under AM 1.5 G irradiation (100 mW cm^{-2}) for $\text{Bi}_2\text{FeCrO}_6$ thin-film solar cells in a multilayer configuration.

Since the discovery of the ferroelectric photovoltaic (FEPV) effect^{1,2}, ferroelectric (FE) materials have been intensely investigated for photovoltaic (PV) applications^{3–7}. Under illumination, FE materials exhibit a short-circuit PV current parallel to the direction of the FE polarization axis^{8–10}, as well as photovoltages that are usually much larger than the bandgap of the material, which is in the range of 3–4 eV for FE oxides with a perovskite structure (that is, ABO_3)^{11,12}. In contrast to the known PV effect of conventional p–n solar cells¹³, with the FEPV effect, photo-excited carriers are transported without the existence of a gradient in the electrochemical potential. The effect is generally believed to be promoted by the polarization-induced internal electric field, also called the depolarization electric field¹⁴. Recent experiments have demonstrated that the power conversion efficiency (PCE) of FE absorber-based PV devices^{3,15} can be considerably enhanced by engineering the FE domain architectures and interfaces and reducing the FE film thickness. Until recently, the FEPV effect remained a scientific curiosity rather than having any real application, because the low conductivity of FE materials resulted in very poor PCE values in devices. To date, despite recent progress in FE oxide engineering and photocurrent extraction methods, a best PCE of ~1.25% has been obtained¹⁶. The wide bandgap (E_g) of FE materials exceeds the ideal value of 1.4 eV (corresponding to the maximum theoretical PCE for a semiconductor PV cell)¹⁷, making them unsuitable for PV applications due to their overall poor sunlight absorption capabilities. This wide bandgap is mainly a result of the fundamental characteristics of the transition metal–oxygen bonds at B sites (cf. Supplementary Fig. 1b) and the large difference in their electronegativities. Thanks to its relatively low bandgap of 2.67 eV, BiFeO_3 (BFO) has been largely investigated for PV applications^{6,18}. However, photons with wavelengths of $\lambda > 464 \text{ nm}$ —accounting for more than 80% of the solar spectrum—cannot be absorbed by BFO, prompting the exploration of new routes to the development of FE materials with semiconducting properties. Lowering the E_g of such oxides without affecting their FE properties is a promising conceptual route to obtain solar energy conversion devices with higher PCE. A lower bandgap of 1.39 eV has been demonstrated recently in FE perovskite $[\text{KNbO}_3]_{1-x}[\text{BaNi}_{1/2}\text{Nb}_{1/2}\text{O}_{3-\delta}]_x$ solid solutions¹⁹. As in LaCoO_3 -doped $\text{Bi}_4\text{Ti}_3\text{O}_{12}$ films²⁰, chemical modification of the transition metal in the perovskite octahedra B sites, which allows E_g to be altered without affecting ferroelectricity^{21,22}, is a promising

way to achieve semiconducting FE perovskites suitable for PV applications. However, the real potential of semiconducting FE perovskites in PV applications is far from being fulfilled.

Here, we demonstrate a new approach to develop active layers promoting efficient perovskite oxide-based PV devices by exploiting the properties of multiferroic $\text{Bi}_2\text{FeCrO}_6$ (BFCO)^{23,24}. Our approach is based on tailoring the Fe/Cr cationic order parameters (R and D , as defined below and in Supplementary Section 1) in the films, leading to effective tuning of absorption and FE properties of BFCO. BFCO crystallizes in a double perovskite structure, where ferroelectricity is driven mostly by the Bi^{3+} ions at A sites (cf. Supplementary Fig. 1b), and E_g is controlled by the interaction between Fe and Cr via O, alternating at B sites. The simultaneous occurrence of these two mechanisms at different sites is the key to fabricate semiconducting FE BFCO oxides with optimal ferroelectricity–optical absorption combinations for efficient PV applications.

Tunable, low-bandgap multiferroic BFCO thin films

The degree of ordering or long-range ordering (LRO) in a double-perovskite structure is controlled by either kinetics or thermal equilibrium depending on the temperature range²⁵. We investigated the effect of Fe/Cr cationic ordering on the optical properties of BFCO by analysing films deposited at several different growth temperatures (from 520 to 720 °C) and various deposition times from 5 to 60 min (Supplementary Fig. 5). The LRO in BFCO films is characterized by (1) the intensity ratio R between the $(\frac{1}{2}\frac{1}{2}\frac{1}{2})$ superstructure reflection and the main (111) perovskite peak, which we determine from the asymmetrical X-ray diffraction (XRD) θ – 2θ scans of the films around the SrTiO_3 (STO)(111) reflection²⁶, and (2) the width of the superlattice peaks, given by the ordered domain size D . The relationship between D and R of the ordered domains in BFCO films is shown in Fig. 1a. At low temperatures and high growth rates, the dependence of D on R is lower than that at low temperatures and low growth rates.

To investigate the effect of R on the absorption properties of BFCO films, we studied samples grown at a low temperature and high growth rate, for which D is almost constant. The high growth rate limits the kinetic effect on LRO, which results in smaller D , typically in the 6–10 nm range (Supplementary Fig. 5a). The obtained BFCO films, labelled N1 to N4, have R values ranging from 0.1 to 0.9% (Supplementary Fig. 5b).

¹NAST Center & Department of Chemical Science & Technology, University of Rome Tor Vergata Via della Ricerca Scientifica, 00133 Rome, Italy,

²INRS—Centre Énergie, Matériaux et Télécommunications, Boulevard Lionel-Boulet, Varennes, Québec, J3X 1S2, Canada, ³Center for Self-Assembled Chemical Structures, McGill University, H3A 2K6 Montreal, Quebec, Canada. *e-mail: nechache@emt.inrs.ca; rosei@emt.inrs.ca

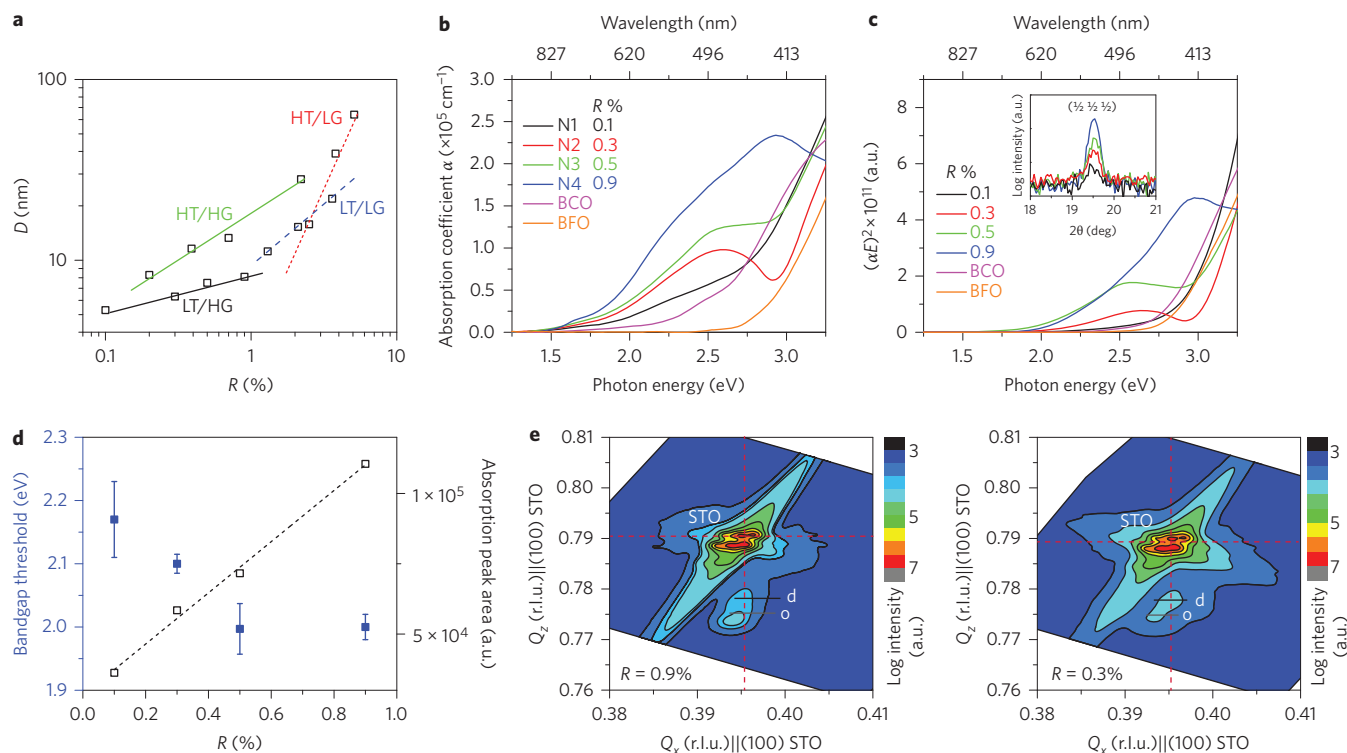


Figure 1 | Structural ordering and optical absorption. **a**, R - D relationship in BFCO films grown under different PLD conditions. **b,c**, UV-visible absorption spectra of BFCO thin films at different R ratio (that is, Fe/Cr cation ordering). HT, high temperature; LT, low temperature; HG, high growth rate; LG, low growth rate. Corresponding absorption coefficients (**b**) and direct optical transitions (**c**). Inset in **c**: normalized XRD intensity of the superstructure peaks. **d**, Bandgap threshold (blue) and corresponding absorption area (black; in arbitrary units, a.u.) at different R in BFCO films. **e**, Reciprocal space maps around STO(204) reflections showing the two spots related to the coexistence of ordered (o) and disordered (d) BFCO phases in films.

Figure 1b presents the absorption coefficient α extracted for the BFCO films, together with that obtained for epitaxial BFO and BiCrO₃ (BCO) films, for comparison. In contrast to the BFO and BCO absorption spectra, peak structures appear between 1.5 and 2.7 eV in the optical absorption spectra of BFCO films, and their intensity increases monotonically with R . In addition, the direct optical transitions illustrated by the $(\alpha E)^2$ versus E plots (Fig. 1c) are characterized by two linear portions, suggesting the presence of two threshold gaps in BFCO films.

Following spin-density functional theory calculations confirmed by absorption spectra of the similar double perovskite La₂FeCrO₆ (ref. 27), we assigned the band in the visible range, ~ 1.99 eV (623 nm), to charge transfer excitations between Cr and Fe mixed d orbital Hubbard transitions that occur in ordered regions of the sample (that is, o-BFCO). The peak area of this band strongly depends on R and thus on Fe/Cr cationic ordering. This is clearly visible in Fig. 1d, which shows the variation of E_g and corresponding areas of ordered regions in BFCO films with R . Although only a small variation of E_g (0.2 eV) is observed with R , we measured a strong dependence (fivefold increase) of the absorption peak area on R . This demonstrates that R is a key parameter that can be used to tailor the amount of absorbed light in BFCO films. The second threshold gap observed near ultraviolet energies ranging from 2.8 to 3.1 eV is close to those of BFO and BCO films, and decreases strongly when Fe/Cr ordering increases in the film ($R = 0.9\%$). These results suggest that in this energy range, absorption in BFCO, BFO and BCO has the same origin, namely O to Fe, O to Cr, and Cr to Cr charge transfers, which take place in disordered BFCO domains (d-BFCO). The presence of two BFCO phases (o-BFCO and d-BFCO) in the films is further confirmed by reciprocal space mappings around the STO(204) reflection, which clearly show two distinct spot reflections (Fig. 1e).

It is known that with annealing time, the B-site cations (Fe/Cr in our case) gain sufficient kinetic energy to migrate to their specific sites to minimize the configurational entropy, which results in the growth of ordered domains²⁸. This modification of spatial ordering distribution obtained through heat treatment is common in many complex perovskite ceramics^{29,30}. Therefore, to investigate the effect of D on the absorption properties of BFCO films, we varied the growth time from 5 to 60 min by adjusting the laser repetition rate f from 2 to 14 Hz. The deposition temperature and oxygen partial pressure were fixed around 580 °C and 10 mTorr, respectively (that is, the low-temperature/low-growth-rate range). The obtained films have an average thickness of ~ 95 nm (Supplementary Table 2). The ordered domain size D of each film was calculated using the Debye-Scherrer formula applied to normalized superlattice $(\frac{1}{2}\frac{1}{2}\frac{1}{2})$ reflections (Fig. 1c, inset).

For this set of samples, films L1 to L4, D varied between 10 nm (film L4, grown at $f = 14$ Hz) and 26 nm (film L1, deposited at $f = 2$ Hz), as shown in Supplementary Fig. 5a. The ratio R for these films did not vary considerably, ranging from 0.45% (film L1) to 0.35% (film L4), so the effect of R on light absorption is minimal. The effect on light absorption of the spatial organization of R (that is, size of D) is shown in Fig. 2a,b. The centre of the absorption bands from the visible range varies within large limits, ranging from ~ 1.75 eV (film L1) to ~ 2.59 eV (film L4). Films L2 and L3 were grown at 6 and 10 Hz, respectively, and exhibit absorption bands centred at 1.97 and 2.25 eV, respectively. On representing the absorption band positions as a function of D for all obtained films (Fig. 2b), a linear dependence with negative slope is observed. This redshift of absorption with increasing D in BFCO films is similar in origin to quantum dot systems, where the characteristic absorption position can be controlled by varying the size of the semiconducting nanostructures³¹. In the present case, the small

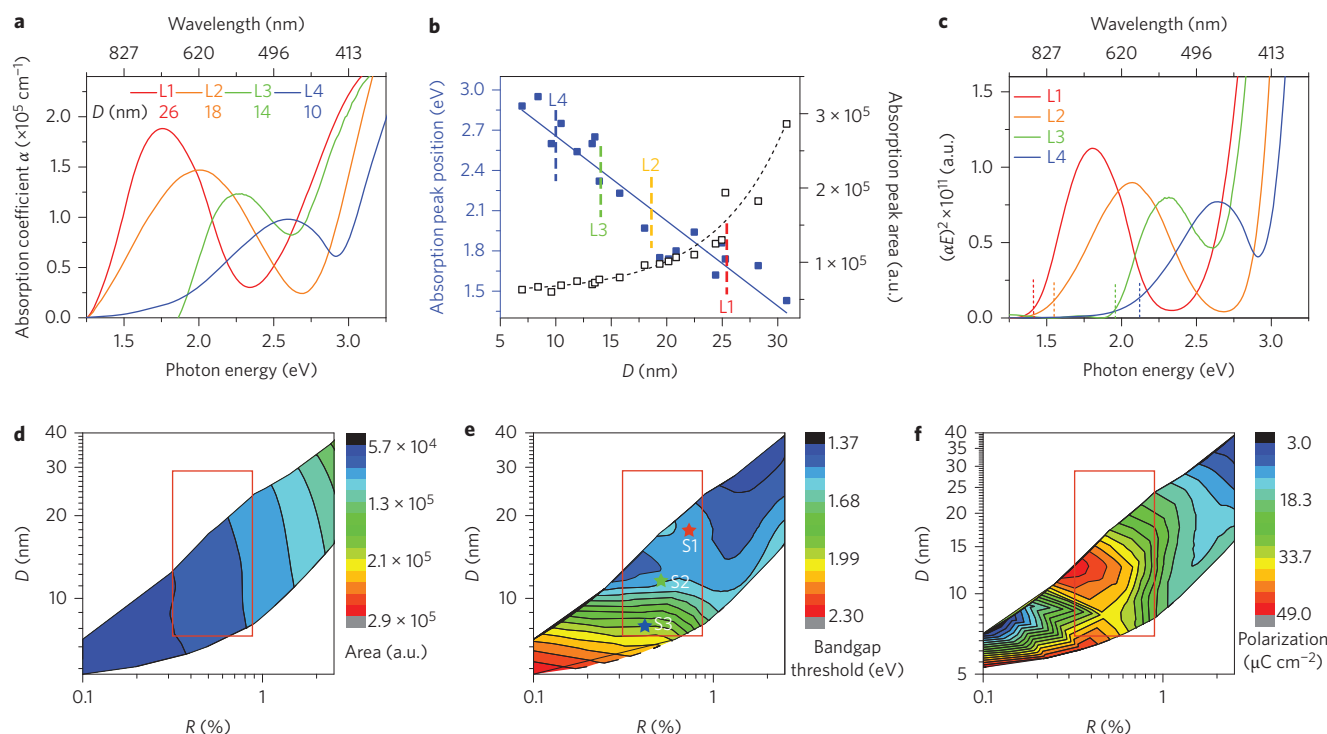


Figure 2 | Effect of cationic ordering on absorption and FE properties. **a**, UV-visible absorption spectra of BFCO thin films. **b**, Absorption peak position (blue) and area (black; in arbitrary units, a.u.) versus ordered BFCO domain size D in films. **c**, Corresponding direct optical transitions of the overall BFCO heterostructures. **d–f**, Mappings of absorption peak area (**d**), bandgap threshold (**e**) and FE polarization (**f**) with ordering characteristics R and D in BFCO films.

ordered domains (low D) are more sensitive to epitaxial strain than the disordered matrix in which they are distributed. We found that the pseudo-cubic unit cell volume of the ordered domain, estimated from asymmetrical reciprocal space mapping (RSM) measurements (Supplementary Fig. 6a), is heavily reduced from 0.0615 nm^3 for films with large D to 0.0602 nm^3 in films with small D . The shrinking BFCO lattice cell results in modification of the Jahn–Teller distortions of the $\text{CrO}_6/\text{FeO}_6$ octahedra, which leads to a decrease in the Cr–O and Fe–O bond distances, contributing to modification of the bandgap, as described in Supplementary Section 1. The region defined by the ordered domains exhibits a bandgap varying from 1.43 to 2.51 eV (Fig. 2c). The second threshold gaps observed in Fig. 1, originating from disordered BFCO regions (between 2.75 and 3.12 eV), are also visible in Fig. 2c. A very low bandgap is therefore achieved in the present films, well below the previously reported values of $\sim 2.7 \text{ eV}$ obtained from a more complex, doped-FE thin-film system ($\text{LaCoO}_3\text{--Bi}_4\text{Ti}_3\text{O}_{12}$; ref. 20), and relatively close to the 1.39 eV obtained very recently by Grinberg and colleagues in weak FE pellets at room temperature (spontaneous polarization $P_s \approx 1 \mu\text{C cm}^{-2}$)¹⁹. Based on these results, we then looked at the combined effect of R and D on the optical properties of BFCO films. The three-dimensional maps in Fig. 2d,e illustrate the dependence of the absorption peak area and its position on LRO parameters R and D .

Due to the crucial role played by FE polarization in the transport of charge carriers, we also assessed the effect of LRO on the remnant polarization, P_r , presented in Fig. 2f. In the range of low R /small D , the bandgap is large (2.3 eV) and no significant effect is observed on polarization, indicating that FE properties, with $P_r \approx 45 \mu\text{C cm}^{-2}$, persist. At high R /large D the bandgap decreases ($E_g \approx 1.4 \text{ eV}$). However, there is also a significant reduction of FE polarization (for details see Supplementary Section 4), which is detrimental for PV performance. Therefore, to achieve efficient BFCO-based PV devices it is essential to balance both bandgap and polarization, the optimal range of LRO parameters being illustrated by the

rectangle shown in the maps (Fig. 2d,e). The BFCO films in this region are characterized by semiconducting bandgaps, good optical absorption and significant FE polarization, which promote the generation and separation of the photocharge carriers.

Photovoltaic properties of single-layer devices

Having clearly established the bandgap tunability in the present films, we subsequently assessed their performance as active layers in PV cells. A series of single-layer oxide PV devices, labelled S1, S2 and S3 (Fig. 2e), were fabricated entirely by pulsed laser deposition (PLD), using SrRuO_3 (SRO) conducting perovskite films as bottom electrodes and two-dimensional arrays of indium tin oxide (ITO) transparent conducting electrodes on top (Fig. 3a). The active layers were deposited at 580°C and at different PLD repetition rates $f = 2, 8$ and 14 Hz , respectively (similar to the L-series films discussed already). The performances of these single layer-based PV devices are presented in Fig. 3b and are summarized in Table 1.

The PCE increases with decreasing growth rate, reaching a value of 3.3% for device S1, with $J_{sc} = 11.7 \text{ mA cm}^{-2}$, $V_{oc} = 0.79 \text{ V}$ and a fill factor (FF) of 0.36. The lowest efficiency (0.5%, FF = 27%) was obtained for device S3. We attribute the increased J_{sc} to enhanced light absorption and possibly to a reduction in the photocharge recombination rate, both promoted by the lower (direct) bandgap. To understand the PV performance of BFCO-based devices and its dependence on polarization, we analysed their electronic structure using ultraviolet photoelectron spectroscopy (UPS).

The energy-level diagrams of each component material used in the BFCO devices are presented in Fig. 3c. A description of the determination of the electron affinity E_e , workfunction E_f and ionization potential E_i is provided in Supplementary Section 5. Due to the complex nature of the ordered/disordered phases in the BFCO films, the energy band diagrams are difficult to construct. Qualitative analyses were performed based on the UPS results obtained for these films, as discussed in Supplementary Section 5.

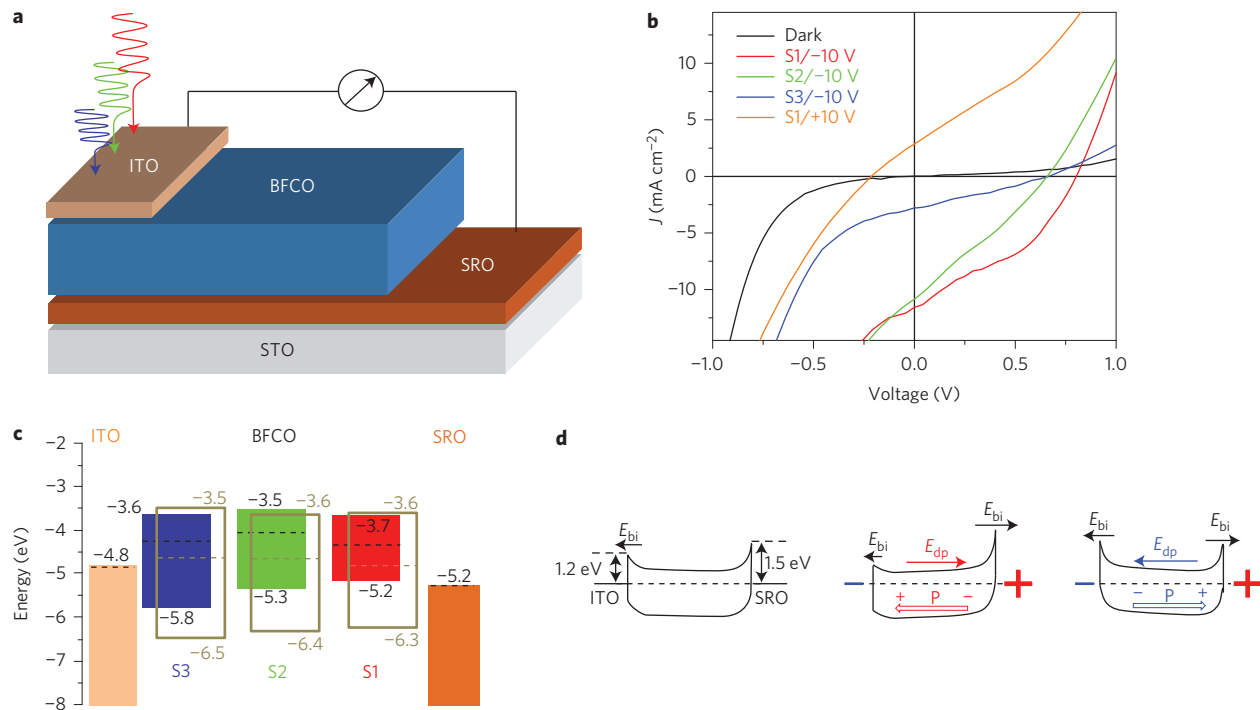


Figure 3 | Single-layer device layout and PV properties. **a**, Device layout of the tested BFCO single-layer-based structure. **b**, J - V characteristics of BFCO single-layer devices under AM1.5G illumination. **c**, Energy-level diagram based on UPS results showing the valence and conduction energies of each of the component materials included in the BFCO device structures. The BFCO part includes empty and filled rectangular shapes relating to disordered and ordered regions, respectively, which coexist in the films. **d**, Schematic of simplified energy band diagrams showing modulation of the Schottky barriers for ITO/BFCO/SRO heteroepitaxial structures, for an ideal metal-semiconductor interface (left) without polarization and for samples negatively and positively poled at ± 10 V (middle and right).

A simplified schematic illustration of the energy band diagrams of the heterostructure is presented in Fig. 3d. The drawing on the left shows the ideal diagram for ITO/BFCO/SRO junctions, in the absence of a net FE polarization (P). During the J - V measurement, a positive voltage was applied to the SRO, resulting in an electric field with opposite direction to the bottom barrier field and in the same direction as the top one. For the case of BFCO films poled positively (+10 V pulse to the SRO electrode), the energy band diagram is modified, as shown in the middle panel of Fig. 3d. Switching the FE polarization by applying a pulse of -10 V to the bottom electrode reverses the sign of V_{oc} and J_{sc} of the device, demonstrating that the FE contribution dominates the PV effect in our devices.

This change is due to modulation of the energy band induced by polarization flipping³². The accumulation of positive (negative) surface charge at the polarization vector head (tail) side shifts the energy levels in the FE down (up), resulting in a reduction (increase) of the barrier height (E_{bi}), which becomes large enough to reverse, for positive poling, the original band bending of the ITO/BFCO/SRO structure (Fig. 3d). The small V_{oc} and J_{sc} measured after negative poling can be explained by the incomplete polarization switching or/and the presence of

recombination sites such as oxygen vacancies that usually exist in such materials.

High-efficiency optimized multilayer devices

The above results clearly demonstrate bandgap tunability via growth and processing optimization. However, the absorption spectrum in devices based on single-layer films is not sufficient to harvest the entire solar radiation spectrum that impinges on the Earth's surface. A natural approach to overcome this limitation is to combine several layers in a single device, each layer being tuned to absorb in a specific region of the solar spectrum, similar to multi-junction PV devices.

As previously shown, BFCO films with large E_g (device S3) are obtained at high deposition rates and under epitaxial strain, and the bandgap shrinks to 1.4 eV (device S1) with strain relaxation and slow film growth. Based on these results (Table 1) we fabricated two multilayer structures composed of three consecutive BFCO layers, deposited on a 35-nm-thick niobium-doped SrTiO₃ (NSTO)-coated, double-side-polished STO substrate, with ITO top electrodes deposited through a mask. We controlled the bandgap of each BFCO layer in this configuration by changing the deposition rate from 2 Hz to 8 Hz and finally to 14 Hz, as shown in Fig. 4c. By choosing this sequence of growth rates we grew the layer with the largest bandgap on top ('front-cell material'), with the lowest-bandgap layer being used as 'rear-cell material', for improved efficiency. The two BFCO multilayer devices were grown at two different temperatures, 580 °C (device M1) and 720 °C (device M2). The dependence of their absorption coefficients on photon energy is presented in Fig. 4a. It can be clearly described as a superposition of the absorption coefficients of the three BFCO single layers (Fig. 2a). The threshold bandgaps of the devices (Fig. 4b) are 1.6 eV (M1) and 1.3 eV (M2), and their broad absorption peaks cover a large fraction

Table 1 | Performance of single layer-based PV devices.

	J_{sc} (mA cm ⁻²)	V_{oc} (V)	FF (%)	PCE (%)
S1	11.7	0.79	36	3.3
S2	10.8	0.65	29	2.1
S3	2.8	0.66	27	0.5
M1	20.6	0.84	47	8.1
M2	23.6	0.56	33	4.3

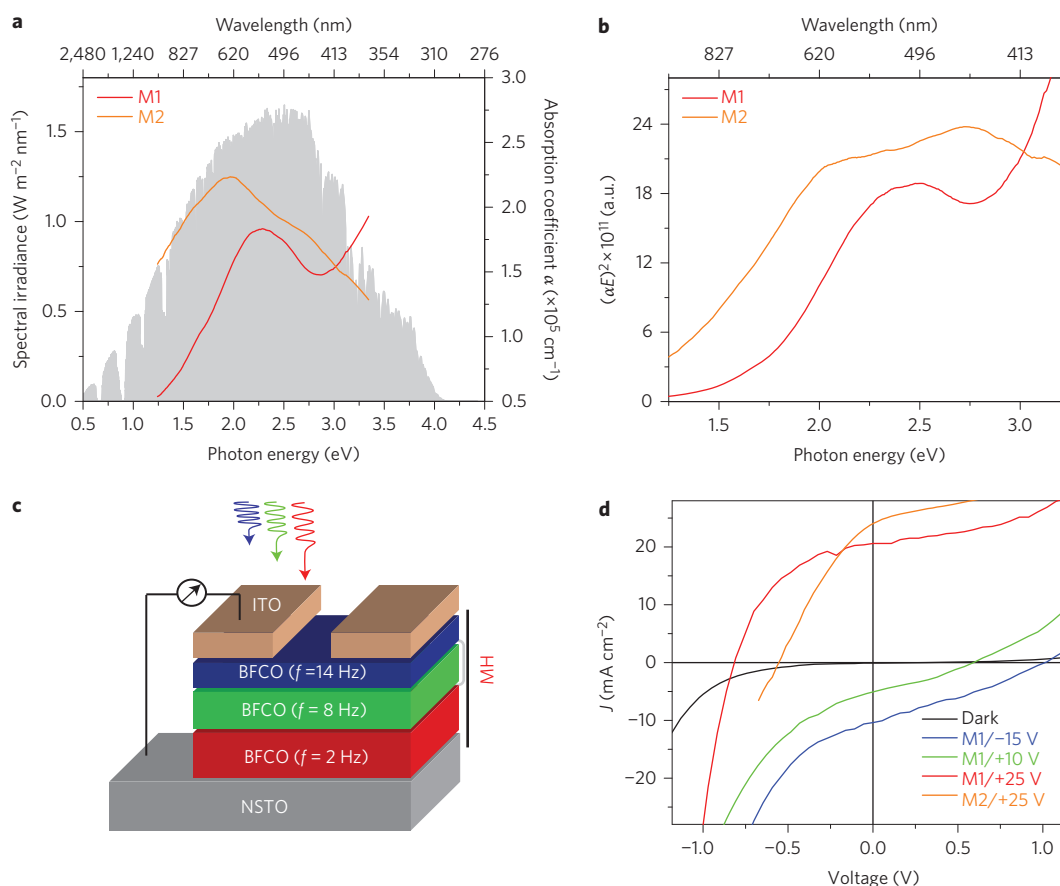


Figure 4 | Optimization of the PV properties of multilayer heterostructure-based devices. **a**, UV-visible absorption profiles of BFCO multilayers (M1 and M2), which indicate that the material absorbs the solar spectrum from 1.4 to 3.2 eV (from 885 to 388 nm) in a complementary manner. **b**, $(\alpha E)^2$ versus energy plots, in arbitrary units (a.u.). **c**, Device geometry of the tested BFCO multilayer structure. **d**, J - V characteristics of BFCO multilayer devices under AM1.5 G illumination.

of the solar spectrum between the visible and ultraviolet regions, leading to a much larger absorption of incident radiation than possible with each individual layer.

Figure 4d presents the J - V curves of the two devices under AM1.5G illumination and after polarization was positively oriented to maximize the FE driving force of the photocharges generated during measurements. As summarized in Table 1, device M1 yielded $J_{\text{sc}} = 20.6 \text{ mA cm}^{-2}$, $V_{\text{oc}} = 0.84$ and $\text{FF} = 0.46$, achieving an unprecedented PCE of 8.1%. The performance parameters for device M2 were $J_{\text{sc}} = 23.6 \text{ mA cm}^{-2}$, $V_{\text{oc}} = 0.56$ and $\text{FF} = 0.33$, with $\text{PCE} = 4.3\%$. To interpret these results we constructed a simplified energy diagram for the band alignment of our ITO/BFCO/NSTO structure, as shown in Fig. 5a. In the absence of polarization the ITO/BFCO/NSTO should behave like a diode with a rectifying current on the positive branch of the J - V curves. This is in contrast with the dark electrical measurement obtained for the as-deposited sample, which highlights the modification of the height barrier at the interfaces mainly induced by the FE polarization. As discussed in the previous section, the polarization switching modulates the energy band of the heterostructure and tailors the direction of the photocurrent and the photovoltage when the device is illuminated. Figure 5b shows the equivalent electrical circuit of the ideal heterostructure for P_{up} (left drawing) and P_{down} (right) states. The total current is the superposition of the dark current I_{d} and the light-generated current I_{L} . The latter flows in the opposite direction to I_{d} and depends on the polarization direction. When the samples are negatively poled, the direction of the photocurrent is reversed and the magnitude of the total current is reduced. This could be explained

by the diffusion current induced in the opposite direction by oxygen vacancies, which can even turn off the PV effect in BFCO films, as previously observed in other perovskites³³. We observed a small number of oxygen vacancies in our films, as evidenced by X-ray photoemission spectroscopy (XPS) measurements (Supplementary Fig. 4). This is, however, below 5%, and so does not significantly affect the unit cell volume.

External quantum efficiency (EQE) measurements of both multilayers are shown in Fig. 5c. M1 exhibits a continuous photoresponse from 380 to 775 nm, with an EQE as high as 58% at 630 nm. In contrast, an interrupted photoresponse is observed for M2, from 680 to 990 nm and from 380 to 660 nm, with a maximum EQE of 20% at 800 nm and 17% at 450 nm, respectively. The EQE of M1 is dramatically reduced to 18% upon switching polarization, confirming its important role in the separation of photogenerated charges. This effect is further established by FE loop measurements (Fig. 5d), revealing that a lower polarization ($\sim 15 \mu\text{C cm}^{-2}$) is obtained for M2 than for M1 ($\sim 35 \mu\text{C cm}^{-2}$).

We have shown that tuning the bandgap in functional perovskite oxides is crucial for the design and development of optoelectronic devices with excellent performances. In particular, reducing the bandgap of the FE film without altering its FE properties is a promising way to achieve solar cells with improved efficiency. In addition to the built-in electric field originating from spontaneous polarization, which can be exploited to efficiently separate the photogenerated electron-hole pairs, the low bandgap enables the number of photons harvested from the broad solar spectrum to be increased and the recombination of charge carriers to be reduced. We

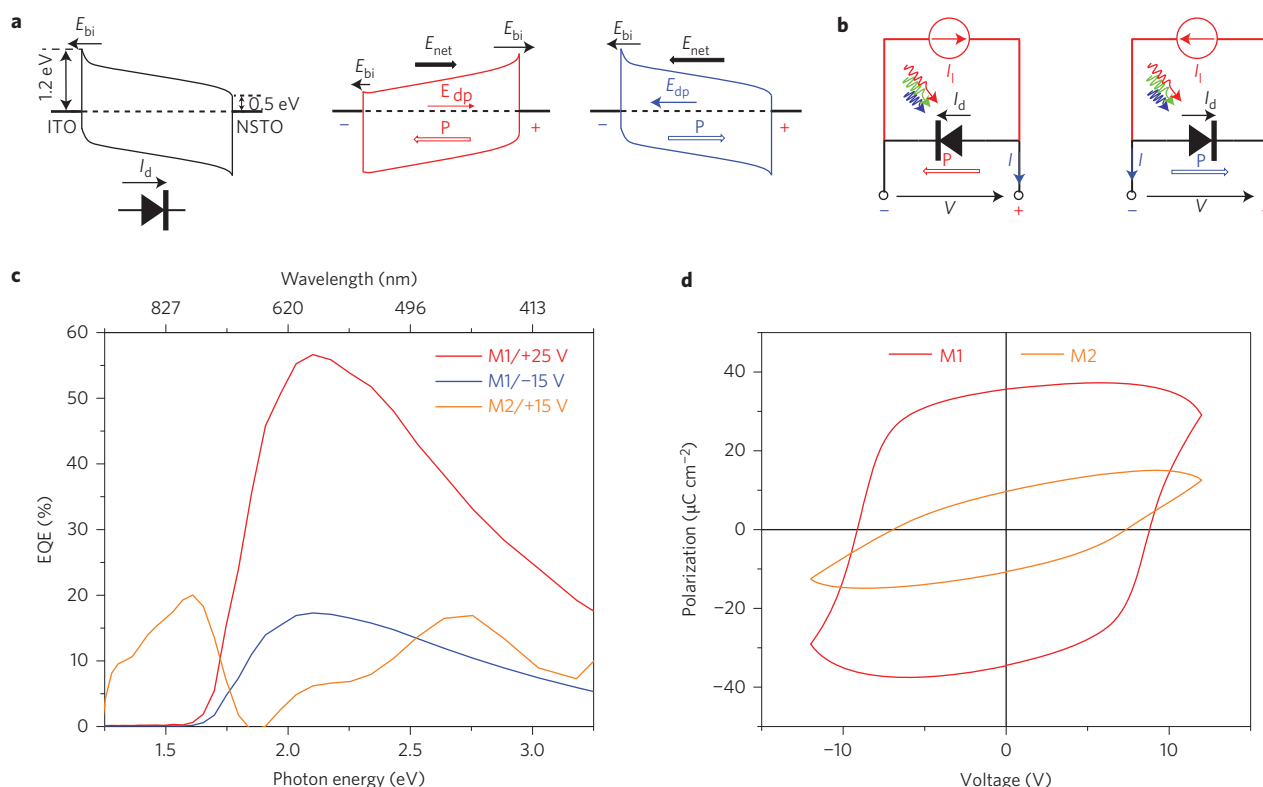


Figure 5 | Multilayer properties and device performance. **a**, Schematics of energy band alignment for the ITO/BFCO/NSTO device, in the absence of polarization (left) and in remnant polarization-up and -down states (right). **b**, Corresponding electrical circuits. **c**, EQE measurements of BFCO multilayers M1 and M2. **d**, Corresponding FE hysteresis loops recorded at 1 kHz and at room temperature.

investigated multiferroic BFCO and established that its electronic bandgap can be tuned to 1.4 eV by tailoring the Fe/Cr cation ordering and the ordered domain size. We demonstrated single and multilayer multiferroic solar cells featuring a low-bandgap BFCO layer with a high efficiency (3.3%) that largely exceeds the performance (1.25%) of previously reported $\text{Pb}(\text{Zr,Ti})\text{O}_3$ (PZT)-based PV devices. We also demonstrated an unprecedented efficiency of 8.1% for optimized multilayer devices. This is a further demonstration of the enormous potential of perovskite-based materials as active layers for efficient PV devices^{34,35}, with an expected PCE as high as 20% in optimized perovskite-based solid-state solar cells³⁶.

Methods

Sample preparation and device fabrication. Thin films were grown epitaxially on both niobium-doped and pristine single-crystal STO(100) substrates by PLD. A stoichiometric BFCO target was ablated using a 240 nm Excimer laser. To promote $\text{Fe}^{2+}/\text{Cr}^{4+}$ cationic order in BFCO thin films (as opposed to $\text{Fe}^{3+}/\text{Cr}^{3+}$), we modified the PLD growth parameters with respect to those previously reported⁴²¹. Films (100 nm thick) were deposited directly on (100)-oriented conducting NSTO substrates. Chemical analysis performed by XPS revealed the formation of valence states 2+ and 4+ for Fe and Cr, respectively, in addition to the 3+ oxidation state (Supplementary Figs 2 and 3). The growth rate was reduced to 0.02 nm/pulse mainly by decreasing the laser fluence from 2.1 to 1.5 J cm⁻². Either SRO or NSTO (Nb, 5 wt%) conducting perovskites were used as the bottom electrode to promote the epitaxial growth of BFCO films and perform electrical measurements. SRO films (20–30 nm thick) were deposited at a substrate temperature of 600 °C and an oxygen partial pressure of 100 mTorr. For the multistack BFCO films, 30- to 45-nm-thick NSTO layers were epitaxially grown at 580 °C and 10 mTorr of oxygen pressure. For comparison we also performed measurements on epitaxial BFO and BCO thin films grown in the same conditions as BFCO. Two-dimensional arrays of transparent 120-nm-thick ITO top electrodes were deposited by PLD through a shadow mask with circular apertures (100–200 μm in diameter).

Thin film characterization. XRD was used to analyse crystal quality and film orientation. Asymmetrical θ - 2θ measurements around STO(111) reflections were performed to qualitatively estimate the cationic ordering between Fe and Cr in BFCO films. RSM measurements were also carried out around the STO(204)

reflection to identify the crystal structure of the obtained films, and to calculate the lattice parameters and the corresponding unit cell volume.

XPS was used to measure the elemental composition and chemical state of the constituents of the BFCO films.

To investigate the absorption properties of the obtained heterostructures, room-temperature variable angle spectroscopic ellipsometry (VASE) measurements were performed in the 1.25–3.35 eV range at five angles of incidence (55, 60, 65, 70 and 75°) using a VASE ellipsometer (J.A. Woollam Company).

The optical constants of BFCO films were determined using spectroscopic ellipsometry. A multilayer model was applied to extract the information contained in the ellipsometric spectra. The model describes the optical response of a system consisting of air, single films or multilayers, bottom electrode and substrate. The data were compared with those obtained for the individual BFO and BCO layers grown in the same conditions. The absorption coefficient α of the films was deduced from the extinction coefficient k using the formula $\alpha = 4\pi k/\lambda$, where λ is the wavelength of incident light. The optical bandgap E_g can be determined from the absorption coefficient α , calculated according to Tauc's relation using the equation $\alpha E = A(E - E_g)^n$, where E is the photon energy, A is a constant, and n is equal to 1/2 or 2 for direct- or indirect-gap materials, respectively. In our data, the lack of the characteristic shape of the $(\alpha E)^{1/2}$ versus E plot and the presence of clear linear slopes in the $(\alpha E)^2$ versus E curves indicate that the bandgap of the films is direct.

As described in detail in the Supplementary Information, UPS was used to estimate the Fermi energies and valence band edges of the materials included in the heteroepitaxial structures.

Single and multilayer PV device measurements. Device characterization was carried out in an ambient environment. The FE properties of BFCO films were measured using a thin-film analyser system at 1 kHz. The same equipment was used to apply pulses to switch the FE polarization. We used $1 \mu\text{s} \pm 10 \text{ V}$ and no relevant change of the result was observed for longer pulses up to 1 ms. For PV measurements, the current–voltage characteristics of the devices were recorded using a Keithley source meter. Illumination of 1 Sun was obtained using an AAA class Sun simulator equipped with 1.5 AM filter with an irradiation intensity of 100 mW cm⁻². The system for device characterization was calibrated with a silicon reference diode. The EQE spectra were acquired under 1.5 AM white light using an EQE 200 Oriel integrated system. The measurement step was 10 nm and the photocurrent was recorded using a lock-in amplifier. The measurement procedure is discussed in more detail in Supplementary Section 6. Complete current–voltage measurements were performed and no hysteretic behaviour was observed (Supplementary Fig. 15). For each type of film/device architecture we prepared and

performed measurements on three to five distinct samples (Supplementary Table 3). We obtained 25% dispersion in efficiency, which we consider to be the cumulative experimental error (including errors in film uniformity, top electrode size, uniformity of the incident light, current and voltage errors).

Received 10 March 2014; accepted 29 September 2014;
published online 10 November 2014

References

- Chynoweth, A. G. Surface space-charge layers in barium titanate. *Phys. Rev.* **102**, 705 (1956).
- Chen, F. S. Optically induced change of refractive indices in LiNbO₃ and LiTaO₃. *J. Appl. Phys.* **40**, 3389 (1969).
- Yang, S. Y. *et al.* Above-bandgap voltages from ferroelectric photovoltaic devices. *Nature Nanotech.* **5**, 143–147 (2010).
- Nechache, R. *et al.* Photovoltaic properties of Bi₂FeCrO₆ epitaxial thin films. *Appl. Phys. Lett.* **98**, 202902 (2011).
- Yuan, Y. *et al.* Efficiency enhancement in organic solar cells with ferroelectric polymers. *Nature Mater.* **10**, 296–302 (2011).
- Alexe, M. & Hesse, D. Tip-enhanced photovoltaic effects in bismuth ferrite. *Nature Commun.* **2**, 256 (2011).
- Nechache, R., Ruediger, A. & Rosei, F. Combined pn junction and bulk photovoltaic device. US patent 13/162,186 (2011).
- Glass, A. M., von der Linde, D. & Negran, T. J. High-voltage bulk photovoltaic effect and the photorefractive process in LiNbO₃. *Appl. Phys. Lett.* **25**, 233–235 (1974).
- Josch, W., Munser, R., Ruppel, W. & Wurfel, P. The photovoltaic effect and the charge transport in LiNbO₃. *Ferroelectrics* **21**, 623–625 (1978).
- Koch, W. T. H., Munser, R., Ruppel, W. & Wurfel, P. Bulk photovoltaic effect in BaTiO₃. *Solid State Commun.* **17**, 847 (1975).
- Robertson, J., Warren, W. L. & Tuttle, B. Band states and shallow hole traps in Pb(Zr,Ti)O₃ ferroelectrics. *J. Appl. Phys.* **77**, 3975 (1995).
- Yang, S., Zhang, Y. & Mo, D. A. Comparison of the optical properties of amorphous and polycrystalline PZT thin films deposited by the sol–gel method. *Mater. Sci. Eng. B* **127**, 117–122 (2006).
- Chanussot, G. Physical models for the photoferroelectric phenomena. *Ferroelectrics* **20**, 37–50 (1978).
- Qin, M., Yao, K. & Liang, Y. C. High efficient photovoltaics in nanoscaled ferroelectric thin films. *Appl. Phys. Lett.* **93**, 122904 (2008).
- Bhatnagar, A., Chaudhuri, A. R., Kim, Y. H., Hesse, D. & Alexe, M. Role of domain walls in the abnormal photovoltaic effect in BiFeO₃. *Nature Commun.* **4**, 2835 (2013).
- Zheng, F. *et al.* Above 1% efficiency of a ferroelectric solar cell based on the Pb (Zr,Ti)O₃ film. *J. Mater. Chem. A* **2**, 1363 (2014).
- Zhang, G. *et al.* New high *T_c* multiferroics KBiFe₂O₅ with narrow band gap and promising photovoltaic effect. *Sci. Rep.* **3**, 1265 (2013).
- Ji, W., Yao, K. & Liang, Y. C. Bulk photovoltaic effect at visible wavelength in epitaxial ferroelectric BiFeO₃ thin films. *Adv. Mater.* **22**, 1763–1766 (2010).
- Grinberg, I. *et al.* Perovskite oxides for visible-light-absorbing ferroelectric and photovoltaic materials. *Nature* **503**, 509–512 (2013).
- Choi, W. S. *et al.* Wide bandgap tunability in complex transition metal oxides by site-specific substitution. *Nature Commun.* **3**, 689 (2012).
- Nechache, R. *et al.* Epitaxial thin films of the multiferroic double perovskite Bi₂FeCrO₆ grown on (100)-oriented SrTiO₃ substrates: growth, characterization, and optimization. *J. Appl. Phys.* **105**, 061621 (2009).
- Xu, X. S. *et al.* Tunable band gap in Bi(Fe_{1-x}Mn_x)O₃ films. *Appl. Phys. Lett.* **96**, 192901 (2010).
- Kamba, S. *et al.* Infrared and magnetic characterization of multiferroic Bi₂FeCrO₆ thin films over a broad temperature range. *Phys. Rev. B* **77**, 104111 (2008).
- Nechache, R. *et al.* Epitaxial patterning of Bi₂FeCrO₆ double perovskite nanostructures: multiferroic at room temperature. *Adv. Mater.* **23**, 1724–1729 (2011).
- Shimada, T., Nakamura, J., Motohashi, T., Yamauchi, H. & Karppinen, M. Kinetics and thermodynamics of the degree of order of the B cations in double-perovskite Sr₂FeMoO₆. *Chem. Mater.* **15**, 4494–4497 (2003).
- Nechache, R., Harnagea, C. & Pignolet, A. Multiferroic properties–structure relationships in epitaxial Bi₂FeCrO₆ thin films: recent developments. *J. Phys. Condens. Matter.* **24**, 096001 (2012).
- Andreasson, J. *et al.* Electron-lattice interactions in the perovskite LaFe_{0.5}Cr_{0.5}O₃ characterized by optical spectroscopy and LDA+U calculations. *Phys. Rev. B* **80**, 075103 (2009).
- Tai, C. W. & Baba-Kishi, K. Z. Influence of annealing on B-site order and dielectric properties of (0.4)Pb(In_{1/2}Nb_{1/2})O₃:(0.6)Pb(Mg_{1/3}Nb_{2/3})O₃ relaxor ceramics. *J. Appl. Phys.* **100**, 116103 (2006).
- Baba-Kishi, K. Z. & Baber, D. J. Transmission electron microscope studies of phase transitions in single crystals and ceramics of ferroelectric Pb(Sc_{1/2}Ta_{1/2})O₃. *J. Appl. Crystallogr.* **23**, 43–54 (1990).
- Perrin, C. *et al.* Influence of B-site chemical ordering on the dielectric response of the Pb(Sc_{1/2}Nb_{1/2})O₃ relaxor. *J. Phys. Condens. Matter* **13**, 10231–10245 (2001).
- Sargent, E. H. Colloidal quantum dot solar cells. *Nature Photon.* **6**, 133–135 (2012).
- Maksymovych, P. *et al.* Polarization control of electron tunneling into ferroelectric surfaces. *Science* **324**, 1421 (2009).
- Guo, Y., Guo, B., Dong, W., Li, H. & Liu, H. Evidence for oxygen vacancy or ferroelectric polarization induced switchable diode and photovoltaic effects in BiFeO₃ based thin films. *Nanotechnology* **24**, 275201 (2013).
- Malinkiewicz, O. *et al.* Perovskite solar cells employing organic charge-transport layers. *Nature Photon.* **8**, 128–132 (2014).
- Liu, D. & Kelly, T. L. Perovskite solar cells with a planar heterojunction structure prepared using room-temperature solution processing techniques. *Nature Photon.* **8**, 133–138 (2014).
- Park, N. G. Organometal perovskite light absorbers toward a 20% efficiency low-cost solid-state mesoscopic solar cell. *J. Phys. Chem. Lett.* **4**, 2423–2429 (2013).

Acknowledgements

The authors acknowledge financial support from the Canada Foundation for Innovation, which funded the facilities for materials deposition and characterization as well as device fabrication and testing. F.R. is grateful to the Canada Research Chairs Program for partial salary support. F.R. is supported by Discovery (NSERC) and FQRNT team grants. This work was partly funded by an international collaboration grant (MDEIE) with the European Network WIROX. F.R. acknowledges the Alexander von Humboldt Foundation for a F.W. Bessel Award. F.R. is grateful to Elsevier for a grant from Applied Surface Science. R.N. is grateful to NSERC for a personal postdoctoral fellowship for partial salary support. S.L. thanks FRQNT and CSC for salary support. L.C. acknowledges partial salary support through a personal fellowship from FRQS.

Author contributions

R.N. designed the materials and device optimization strategy. R.N., S.L. and J.C. fabricated and characterized the structural, composition, FE and photovoltaic properties of the films. R.N. and L.C. performed UPS analysis. R.N., W.H. and S.L. carried out the NSTO deposition and electrical and optical measurements for the devices. R.N. and C.H. designed the piezoresponse force microscopy experiments and supervised the analysis of the results and their interpretation. R.N., C.H. and F.R. co-wrote the paper. F.R. supervised the work.

Additional information

Supplementary information is available in the [online version](#) of the paper. Reprints and permissions information is available online at www.nature.com/reprints. Correspondence and requests for materials should be addressed to R.N. and F.R.

Competing financial interests

R.N. and F.R. declare that a US patent related to the PV properties of BFCO films was filed in 2011 under reference 13/162,186.